
Article:
Chen, L. and de Borst, R. orcid.org/0000-0002-3457-3574 (2021) Phase-field modelling of cohesive fracture. European Journal of Mechanics - A/Solids, 90. 104343. ISSN 0997-7538

https://doi.org/10.1016/j.euromechsol.2021.104343

Phase-field modelling of cohesive fracture

Lin Chen[a], René de Borst[a,*]

[a] *University of Sheffield, Department of Civil and Structural Engineering, Sir Frederick Mappin Building, Mappin Street, Sheffield S1 3JD, UK*

Abstract

In phase-field models the damage evolution problem is considered as a minimisation problem of a Griffith-like energy functional, governed by the principles of irreversibility, stability and energy balance. Herein, we consider phase-field models characterised by different degradation and energy dissipation functions. With a proper choice for the characteristic functions in phase-field models, it is possible to reproduce cohesive fracture in a one-dimensional setting. We consider a one-dimensional bar with stress softening, which exhibits homogeneous deformations provided that the length of the bar length is below a state-dependent critical value. Otherwise, the bar will lose stability and show a localised response. It appears that the phase-field method can partially reproduce the response of a cohesive zone model, for instance the traction-separation law, but not all aspects of the model, like the dissipated energy. For a one-dimensional problem, the crack nucleation load varies smoothly from that predicted by a strength criterion to that of a toughness criterion for different lengths of the bar. We have compared the one-dimensional results with the numerical solutions in a two-dimensional setting, which yielded a very good agreement.

Keywords: phase-field model; cohesive-zone model; variational method; stability; smeared-crack models.

1. Introduction

The numerical simulation of fracture is a technically relevant and scientifically challenging issue, and has been a focal point of attention since the early simulations in the 1960s [1, 2], e.g., [3, 4] for overviews. From the very beginning, two different approaches have been pursued, namely discrete methods, in which cracks are treated as discontinuities in the domain [5–12], and distributed, or smeared approaches, in which a discontinuity is modelled by distributing it over a small, but finite band with concomitant high local strains, e.g. [2]. Later, the smeared approaches were cast in a damage format, e.g. [13], and more recently, phase-field models have been introduced to describe brittle fracture in a smeared manner [14–17]. The close relation between phase-field models for brittle fracture and gradient-enhanced continuum damage models has recently been discussed in detail [18].

The phase-field approach to brittle fracture finds its origins in the so-called variational approach to fracture [14]. Herein, crack initiation and quasi-static propagation were considered as a minimisation problem of a Griffith-like energy functional. To make the problem amenable to large-scale computations a regularisation strategy was developed subsequently, which transforms the sharp crack into a distributed crack, governed by a phase-field variable d. The width of the distributed crack is set by an internal length scale ℓ [19]. The resulting functional contains first-order derivatives of the phase-field variable. This fits naturally in a standard C^0 Galerkin approach, and therefore enables the use of standard finite element procedures.

The vast majority of phase-field models have been applied to the analysis of brittle fracture in materials with an isotropic surface energy, e.g. [19–22]. Nevertheless, many natural and man-made materials have an anisotropic surface energy owing to their microstructure, for instance caused by the manufacturing process. This anisotropic character can significantly influence the crack path, for instance in single crystals, in geological materials, in rolled aluminium alloy plates, in fibre-reinforced composites, or in extruded polymers. The resulting functional includes second-order derivatives, necessitating C^1-continuity of the interpolation functions. Numerical simulations have been

*Corresponding author
Email address: r.deborst@sheffield.ac.uk (René de Borst)

carried out using meshfree discretisations, T-splines, and Powell-Sabin B-splines [23–25], and appear capable of reproducing the experimentally observed crack patterns.

Indeed, phase-field models are very promising for simulating fracture and have proven their value in brittle crack propagation. However, the extension to cohesive fracture is underdeveloped. Verhoosel and de Borst [26] proposed an auxiliary field to model the crack opening which is required as input in a cohesive-zone model, see also [27–29]. Nguyen et al. [30] avoided an auxiliary field by computing the crack opening at two points near the crack path. However, the choice of the location of these points is questionable and problem-dependent. Another approach to model cohesive fracture is the phase-field regularised cohesive-zone model. It modifies the degradation function and the homogeneous energy dissipation function [21, 31, 32]. The surface energy functional is the same as that for brittle fracture, while the cohesive zone law is reproduced in a one-dimensional setting. There is also some work on the computation of the crack opening from the deformations in the localised zone. For instance, Yoshioka and co-workers [33, 34] employed an integration approach to obtain the crack opening in their analysis of hydraulic fracturing in porous media.

So far, work on phase-field regularised cohesive-zone models deals exclusively with special choices of the degradation function and the homogeneous energy dissipation function. This study will address the general case of phase-field regularised cohesive-zone models, and deal with a large class of elastic-softening materials. We focus on the stability of the homogeneous response of a bar. The bar will lose stability and show a localised response for sufficiently long bars. Such localised solutions yield the response in cohesive zone models.

We will start this contribution with a concise description of cohesive zone models and phase-field approximations of brittle fracture. Subsequently, the convergence of phase-field model towards a cohesive zone model is studied. The finite element implementation of the model is briefly discussed in Section 5. Finally, a numerical example is presented to validate the approach and conclusions are drawn.

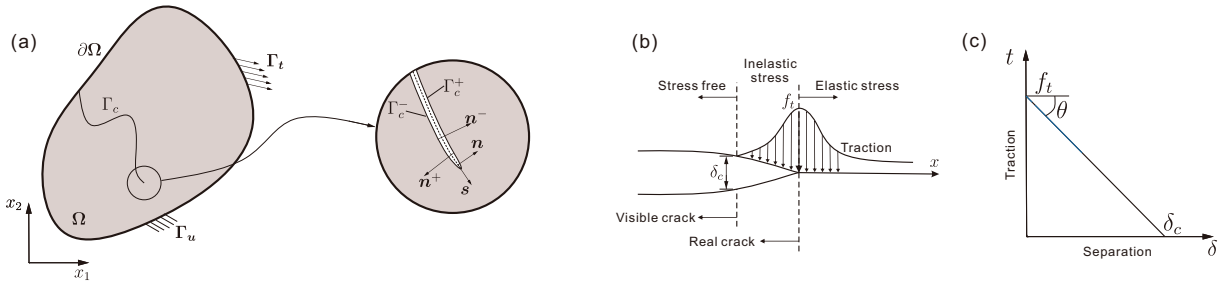

Figure 1: (a) A solid body $\mathbf{\Omega}$ with an internal discontinuity Γ_c; Γ_c is an interface boundary with positive and negative sides, Γ_c^+ and Γ_c^-, respectively; (b) Fracture process zone around the crack tip; (c) Linear cohesive zone law.

2. Cohesive zone model

Cohesive-zone models [35, 36] are nowadays widely employed to model fracture, especially in quasi-brittle and ductile materials [4, 37] and have been incorporated in advanced discretisation technologies [10, 11, 38]. Cohesive-zone models essentially relate the tractions on a lower dimensional crack surface Γ_c in a three-dimensional or two-dimensional body to the crack separation, see Figure 1(a). This so-called traction-separation (cohesive zone) law is given by:

$$\mathbf{t}_d = \mathbf{t}_d\left(\llbracket \boldsymbol{v} \rrbracket\right), \tag{1}$$

where, in a two-dimensional setting, $\mathbf{t}_d = (t_s,\, t_n)^{\mathrm{T}}$ contains the tractions acting on the crack surface and $\llbracket \boldsymbol{v} \rrbracket$ gives the crack separation. Both are defined in the local coordinate system $(s,\, n)$, see Figure 1(a).

In the current study, we only consider crack opening (mode-I fracture), hence we ignore the crack sliding or the shear effect. In the cohesive-zone model, the fracture process zone localises, as a consequence of softening, into a narrow band ahead of the visible crack, see Figure 1(b). A range of different traction-opening relations have been proposed, with applications ranging from ductile to quasi-brittle fracture. Important parameters are the fracture strength f_t, which is the maximum traction exerted on the interface Γ_c, and the fracture energy $\mathcal{G}_c$, which is the amount

of energy needed to create a unit area of cracked surface. But also the shape of the decohesion curve can significantly affect the fracture process.

Two versions of the cohesive-zone model are commonly employed, those of Dugdale [35] and Barenblatt [36]. In Dugdale's approach, the traction-separation relation is defined as

$$t(\delta) = f_t \qquad \mathcal{G}(\delta) = f_t\delta \qquad \text{for} \qquad \delta \le \delta_c = \frac{\mathcal{G}_c}{f_t} \qquad \text{else} \qquad \mathcal{G}(\delta) = \mathcal{G}_c \tag{2}$$

where δ is the crack separation, $t(\delta)$ gives the traction on the crack surface, $\mathcal{G}(\delta)$ indicates the dissipated energy per unit of surface, and δ_c is the crack separation at which cohesive forces cease to exist. Dugdale's model is a constant traction model, similar to the rigid/perfectly-plastic model, but with a cut-off value δ_c. In Barenblatt's model a linear descending branch is used to describe the traction-separation relation (Figure 1(c)):

$$t(\delta) = f_t\left(1 - \frac{f_t\delta}{2\mathcal{G}_c}\right) \qquad \mathcal{G}(\delta) = f_t\delta - \frac{f_t^2\delta^2}{4\mathcal{G}_c} \qquad \text{for}\delta \le \delta_c = \frac{2\mathcal{G}_c}{f_t} \qquad \text{else} \qquad \mathcal{G}(\delta) = \mathcal{G}_c \tag{3}$$

Other cohesive-zone laws, incorporating for instance an exponentially descending branch, can be derived easily.

The cohesive-zone relation is given in the setting of a discrete crack model, with a discrete crack surface Γ_c, see Figure 1(a). In the next section, we will derive the cohesive relation in a smeared-crack model exploiting the phase-field method. In particular, we will present the construction of Barenblatt's version of the cohesive-zone model, and argue that it is not possible to build Dugdale's version of the cohesive-zone model within the framework of the phase-field method.

3. Variational formulation of phase field model

The variational approach to fracture was proposed by Francfort and Marigo [14]. In their work, the crack initiation and quasi-static crack evolution are considered as the minimisation of a Griffith-like energy functional. Here, we consider a cracked body $\Omega \subseteq \mathcal{R}^n$ with a prescribed displacement $\bar{\mathbf{u}}$ on $\partial\Omega_u$ and a prescribed traction $\bar{\mathbf{t}}$ on $\partial\Omega_t$. Then, the energy functional for the cracked body reads

$$\mathcal{E}(\mathbf{u}, \Gamma) = E_u(\mathbf{u}, \Gamma) + E_s(\Gamma) = \int_{\Omega\setminus\Gamma} \mathcal{W}(\mathbf{u})\,\mathrm{d}\Omega + \mathcal{G}_c \int_\Gamma \mathrm{d}\mathcal{H}^{n-1}, \tag{4}$$

where $E_u(\mathbf{u}, \Gamma)$ is the elastic energy stored in the cracked body and $\mathcal{W}(\mathbf{u})$ is the energy density function. Herein, we consider isotropic linear elasticity, so that $\mathcal{W}(\mathbf{u}) = \mu\boldsymbol{\varepsilon}(\mathbf{u}) \cdot \boldsymbol{\varepsilon}(\mathbf{u}) + \lambda/2\mathrm{tr}(\boldsymbol{\varepsilon}(\mathbf{u}))^2$ with $\boldsymbol{\varepsilon}(\mathbf{u}) = 1/2\left(\nabla\mathbf{u} + \nabla\mathbf{u}^{\mathrm{T}}\right)$, and λ and μ are the Lamé constants, and $\cdot$ denotes the inner product. $E_s(\Gamma)$ represents the fracture surface energy in the sense of Griffith's theory of brittle fracture, $\mathcal{H}^{n-1}$ denotes the $(n-1)$-dimensional Hausdorff surface measure, and Γ is the set of cracks where the displacement fields $\mathbf{u} \in H^1(\Omega \setminus \Gamma)$ can jump. $H^1(\Omega \setminus \Gamma)$ is the Sobolev space of functions with square integrable first derivatives. $\mathcal{G}_c$ has the dimensions of an energy per unit of surface.

Direct numerical implementation of Griffith's energy functional (4) is challenging because of unknown location of the displacement jump. Therefore, a regularisation strategy was proposed [19]. In the regularised framework, cracks are represented by a scalar phase field variable d, ranging from 0 (away from the crack) to 1 (completely broken state). d varies smoothly in a band of finite width, resulting in a smeared version of the crack model. The energy functional, Equation (4), is thus replaced by the functional:

$$\mathcal{E}_\ell(\mathbf{u}, d) = \int_\Omega a(d)\,\mathcal{W}(\mathbf{u})\,\mathrm{d}\Omega + \frac{\mathcal{G}_c}{c_\omega}\int_\Omega \left(\frac{\omega(d)}{\ell} + \ell\|\nabla d\|^2\right)\mathrm{d}\Omega, \tag{5}$$

where $a(d)$ denotes a degradation function with a reciprocal function $s(d) = 1/a(d)$, $\omega(d)$ is an increasing function which represents the homogeneous energy dissipation per unit of volume, $\mathcal{G}_c$ is the critical energy release rate or fracture toughness, and $c_\omega = 4\int_0^1 \sqrt{\omega(d)}\,\mathrm{d}d$ is a normalisation parameter. A regularisation length $\ell > 0$ is introduced to govern the width of the distributed crack. If $\ell \to 0$, the regularised model converges to the variational theory of sharp brittle fracture in the sense of Γ-convergence [19].

In this contribution, we consider $a(d)$ and $\omega(d)$ to be non-negative and (at least) twice continuously differentiable functions on $[0,\ 1)$. In addition, they should satisfy [39]:

$$\begin{aligned}
&\text{Positive elasticity:} && a(d) \in [0,\ 1] \quad \text{and} \quad s(d) \in [1, +\infty) && \text{(6a)}\\
&\text{Decreasing elasticity:} && a'(d) \leq 0 \quad \text{and} \quad s'(d) > 0 && \text{(6b)}\\
&\text{Dissipation:} && \omega(d) \in [0,\ 1] \quad \text{and} \quad \omega'(d) \geq 0 && \text{(6c)}\\
&\text{Stress softening:} && \omega'(d)s''(d) - \omega''(d)s'(d) > 0 && \text{(6d)}
\end{aligned}$$

which conditions will be required to hold when constructing a phase-field regularised cohesive-zone model. Equation (6d) signifies that the stress decreases when the damage (d) develops. It can be derived from Equation (21), see also [39] for a physical interpretation. Table 1 shows three commonly employed phase-field models which satisfy these requirements [17, 19, 21].

To meet the stress softening assumption in Equation (6d), Lorentz [40] and Pham [41] derived an upper bound for the regularisation length $\ell \leq 3\ell_{\text{ch}}/2\,(p+2)$ with $\ell_{\text{ch}} = E_0\mathcal{G}_c/f_t^2$ the characteristic length scale and $p = -0.5$ a shape parameter. The derivation is based on the assumption $\omega(d) = d$ and setting $s''(d) > 0$. However, this does not hold for model PCM in Table 1. Model PCM satisfies the stress-softening assumption automatically, which is different from the restriction on the regularisation length in [42].

Table 1: Phase-field models used in this work ($m = 4\ell_{\text{ch}}/\pi\ell$, $p = -0.5$).

Model	$a(d)$	$\omega(d)$	c_ω	σ_e
AT1 [19, 43]	$(1-d)^2$	d	$\frac{8}{3}$	f_t
AT2 [17, 43]	$(1-d)^2$	d^2	2	0
PCM [21]	$\frac{(1-d)^2}{(1-d)^2+md(1+pd)}$	$2d-d^2$	π	f_t

We denote $\bar{\mathbf{u}}_t$ and $\bar{\mathbf{t}}_t$ as the imposed displacement and the prescribed tractions on the boundaries $\partial\Omega_u$ and $\partial\Omega_t$, respectively, at time t. We define the space of kinematically admissible displacement field $\mathbf{u}$ at time t as:

$$C\left(\mathbf{u}_t\right) = \left\{\mathbf{v} \in \left(H^1\left(\Omega\right)\right) : \mathbf{v} = \bar{\mathbf{u}}_t \quad \text{on} \quad \partial\Omega_u\right\} \tag{7}$$

with the associated linear space $C_0 = \left\{\mathbf{v} \in \left(H^1\left(\Omega\right)\right) : \mathbf{v} = \mathbf{0} \quad \text{on} \quad \partial\Omega_u\right\}$. Similarly, the admissible phase field is defined as a convex subset of the Sobolev space $\left(H^1\left(\Omega\right)\right)$:

$$\mathcal{P}_t = \left\{\beta \in \left(H^1\left(\Omega\right)\right) : \beta\left(x\right) \in [0,\ 1] \text{ for almost all } x\right\} \tag{8}$$

where the admissible phase field is left free at the boundary, i.e. without specifying Dirichlet boundary conditions. The Neumann boundary conditions will automatically appear through the variational formulation, see Equation (5). For any pair $(\mathbf{u},\ d) \in \left(C\left(\mathbf{u}_t\right),\ \mathcal{P}_t\right)$ at time t, in the absence of body forces, the total energy is given as:

$$\mathcal{E}_t = \mathcal{E}_\ell\left(\mathbf{u}, d\right) - \int_{\partial\Omega_t} \bar{\mathbf{t}}_t \cdot \mathbf{u}\, \mathrm{d}\Gamma \tag{9}$$

We consider the undamaged state at $t = 0$ and formulate the damage evolution problem as [39]:

$$\begin{gathered}
\text{For each } t > 0, \text{ find } \left(\mathbf{u}_t,\ d_t\right) \in \left(C\left(\mathbf{u}_t\right),\ \mathcal{P}_t\right) \text{ such that}\\
\left(\dot{\mathbf{u}}_t,\ \dot{d}_t\right) \in \left(C\left(\dot{\mathbf{u}}_t\right),\ \mathcal{P}\right) \qquad \text{and} \qquad \forall\left(\mathbf{v},\ \beta\right) \in \left(C\left(\dot{\mathbf{u}}_t\right),\ \mathcal{P}\right)\\
d\mathcal{E}\left(\mathbf{u}_t,\ d_t\right)\left(\mathbf{v} - \dot{\mathbf{u}}_t,\ \beta - \dot{d}_t\right) \geq 0
\end{gathered} \tag{10}$$

with the irreversibility condition $\dot{d} \geq 0$ and the initial condition $d_0 = 0$. Here and henceforth, a superimposed dot denotes the derivative with respect to t. The concept of time t corresponds to a quasi-static time setting. $\mathcal{P}$ represents

the convex cone of positive phase-field rates:

$$\mathcal{P} = \left\{\beta \in \left(H^1(\Omega)\right) : \beta(x) \geq 0 \qquad \text{for almost all } x\right\} \tag{11}$$

and $d\mathcal{E}(\mathbf{u},\, d)(\mathbf{v},\, \beta)$ denotes the Gâteaux derivative of $\mathcal{E}(\mathbf{u},\, d)$ in the direction $(\mathbf{v},\, \beta)$:

$$d\mathcal{E}(\mathbf{u},\, d)(\mathbf{v},\, \beta) = \int_\Omega a(d)\frac{\partial \mathcal{W}(\mathbf{u})}{\partial \varepsilon(\mathbf{u})} \cdot \nabla \mathbf{v}\, \mathrm{d}\Omega + \int_\Omega \left(\mathcal{W}(\mathbf{u})a'(d) + \frac{\mathcal{G}_c}{c_\omega \ell}\omega'(d)\right)\beta\, \mathrm{d}\Omega + \frac{\mathcal{G}_c}{c_\omega}\int_\Omega \ell \nabla d \cdot \nabla \beta\, \mathrm{d}\Omega \tag{12}$$

We now choose $\beta = \dot{d}_t$ and $\mathbf{v} = \dot{\mathbf{u}}_t + \mathbf{v}_0$ with $\mathbf{v}_0 \in C_0$ in the variational inequality, Equation (10) [39]. This leads to the standard equilibrium equation:

$$\operatorname{div} \sigma(\varepsilon(\mathbf{u}_t),\, d_t) = 0 \quad \text{in} \quad \Omega, \qquad \sigma \cdot \mathbf{n} = \bar{\mathbf{t}} \quad \text{on} \quad \partial_t \Omega, \tag{13}$$

where the stress $\sigma(\varepsilon(\mathbf{u}_t),\, d_t) = a(d_t)\partial \mathcal{W}(\mathbf{u}_t)/\partial \varepsilon(\mathbf{u}_t)$. The damage evolution problem now reads:

$$\text{Irreversibility:} \qquad \dot{d}_t \geq 0 \qquad d_0 = 0 \quad \text{on} \quad \Omega, \tag{14a}$$

$$\text{Damage criterion:} \qquad \mathcal{W}(\mathbf{u}_t)\, a'(d_t) + \frac{\mathcal{G}_c}{c_\omega \ell}\omega'(d_t) - \frac{\mathcal{G}_c}{c_\omega}\ell \Delta d_t \geq 0 \quad \text{on} \quad \Omega, \tag{14b}$$

$$\text{Energy balance:} \qquad \dot{d}_t\left(\mathcal{W}(\mathbf{u}_t)\, a'(d_t) + \frac{\mathcal{G}_c}{c_\omega \ell}\omega'(d_t) - \frac{\mathcal{G}_c}{c_\omega}\ell \Delta d_t\right) = 0 \quad \text{on} \quad \Omega, \tag{14c}$$

$$\text{Boundary conditions:} \qquad \frac{\partial d_t}{\partial \mathbf{n}} \geq 0 \qquad \text{and} \qquad \dot{d}_t \frac{\partial d_t}{\partial \mathbf{n}} = 0 \quad \text{on} \quad \partial\Omega \tag{14d}$$

with $\mathbf{n} = (n_1,\, n_2)$ normal vector to the boundary $\partial\Omega$.

At each time t we consider the stability of the system, as given by [41]:

$$\begin{aligned} &\text{For each } t > 0,\ \forall\, (\mathbf{v},\, \beta) \in (C_0,\, \mathcal{P}), \quad \exists \bar{h} > 0 : \forall h \in \left[0,\, \bar{h}\right], \\ &(\mathbf{u}_t + h\mathbf{v},\, d_t + h\beta) \in (C(\mathbf{u}_t),\, \mathcal{P}_t), \quad \mathcal{E}(\mathbf{u}_t + h\mathbf{v},\, d_t + h\beta) \geq \mathcal{E}(\mathbf{u}_t,\, d_t) \end{aligned} \tag{15}$$

4. Convergence of phase field model toward cohesive zone model

In this section, we will construct the cohesive response of a phase-field model. We begin with a closed-form solution in a one-dimensional (1D) context. With the internal parameters in the phase-field model, the elastic stiffness, the fracture energy and the fracture strength, the closed-form solution yields several properties of the cohesive-zone model: the fracture strength, the crack separation, and the initial slope of the traction-separation curve.

Setup of the 1D problem: We consider a homogeneous bar with stress softening. The bar is fixed at $x = 0$ and a displacement is imposed at $x = L$: $U_t = tL$. Thus, the Dirichlet and initial conditions read:

$$u_t(x = 0) = 0 \qquad u_t(x = L) = U_t = tL \qquad u_0(x) = 0 \tag{16}$$

where u_0 is the displacement field at $t = 0$. The total energy, cf. Equation (9), is now given by:

$$\mathcal{E}_t(u, d) = \int_0^L \left(\frac{1}{2}a(d)E_0\, u'^2 + \frac{\mathcal{G}_c}{c_\omega}\left(\frac{\omega(d)}{\ell} + \ell d'^2\right)\right) \mathrm{d}x \tag{17}$$

with E_0 the elastic modulus of the bar and $(\cdot)' = \mathrm{d}(\cdot)/\mathrm{d}x$. The bar is assumed to have a unit cross sectional area. For the 1D case, we define the stiffness function $E(d) = a(d)E_0$, with its compliance function $S(d) = 1/E(d)$. Correspondingly, for $\forall x \in (0,\, L)$, the equilibrium equation (13) and the damage evolution equations (14) can be

reformulated as:

$$\text{Equilibrium:} \qquad \sigma_t'(x) = 0 \qquad \sigma_t(x) = a(d) E_0 u', \tag{18a}$$

$$\text{Irreversibility:} \qquad \dot{d}_t \geq 0 \qquad d_0 = 0, \tag{18b}$$

$$\text{Damage criterion:} \qquad \frac{1}{2} E'(d_t)\, u'^2 + \frac{\mathcal{G}_c}{c_\omega \ell} \omega'(d_t) - \frac{\mathcal{G}_c}{c_\omega} \ell d_t'' \geq 0, \tag{18c}$$

$$\text{Energy balance:} \qquad \dot{d}_t \left(\frac{1}{2} E'(d)\, u'^2 + \frac{\mathcal{G}_c}{c_\omega \ell} \omega'(d_t) - \frac{\mathcal{G}_c}{c_\omega} \ell d_t'' \right) = 0, \tag{18d}$$

$$\text{Boundary conditions:} \qquad d_t'(0) \leq 0 \qquad d_t'(L) \geq 0 \tag{18e}$$

which yields a constant stress σ_t along the bar:

$$\sigma_t = \frac{U_t}{\int_0^L S\,(d_t(x))\,\mathrm{d}x} \tag{19}$$

4.1. Homogeneous solutions and the issue of stability

If the phase field and strain field are constant in space and evolve smoothly in time we will obtain a homogeneous solution of the evolution problem. Then, the solution of the equilibrium equation and the damage evolution read:

$$\text{Equilibrium equation solution:} \qquad u_t'(x) = t \qquad u_t(x) = tx \qquad \sigma_t = tE(d_t) \qquad d_t = \text{constant} \tag{20a}$$

$$\text{Damage evolution problem solution:} \qquad \frac{1}{2} E'(d)\, u'^2 + \frac{\mathcal{G}_c}{c_\omega \ell} \omega'(d_t) \geq 0 \qquad \dot{d}_t \left(\frac{1}{2} E'(d)\, u'^2 + \frac{\mathcal{G}_c}{c_\omega \ell} \omega'(d_t) \right) = 0 \tag{20b}$$

From Equation (20), the elastic limit is obtained by setting the phase-field value $d_t = 0$:

$$\sigma_e = \sqrt{\frac{2\mathcal{G}_c}{c_\omega \ell} \frac{\omega'(0)}{S'(0)}} \qquad U_e = \frac{L}{E_0} \sqrt{\frac{2\mathcal{G}_c}{c_\omega \ell} \frac{\omega'(0)}{S'(0)}} \qquad t_e = \frac{U_e}{L} \tag{21}$$

with U_e the end displacement at $x = L$ and t_e the corresponding time step. From this it can be shown that the models AT1 and PCM have an elastic phase with a non-zero stress limit, but this does not hold for model AT2. When the end displacement U_t at time t exceeds U_e the bar will be damaged homogeneously and Equation (20b) will become an equality, which yields:

$$\sigma_t = \sqrt{\frac{2\mathcal{G}_c}{c_\omega \ell} \frac{\omega'(d_t)}{S'(d_t)}} \qquad U_t = \frac{L}{E(d_t)} \sqrt{\frac{2\mathcal{G}_c}{c_\omega \ell} \frac{\omega'(d_t)}{S'(d_t)}} \tag{22}$$

Due to the stress softening requirement, Equation (6d), the stress σ_t is now monotonically decreasing. Of course, it is in practice impossible to carry out experimental tests such that the bar continued to deform homogeneously.

The homogeneous solution $(tx,\, d_t)$ satisfies the equilibrium equation and the damage evolution equation, Equation (18). However, the solution $(tx,\, d_t)$ maybe not stable. To perform a stability analysis we need to express Equation (15) in a Taylor series [41] and analyse the sign of the first and second derivatives of the total energy. For a 1D case the first and second derivatives are expressed in a general format as:

$$d\mathcal{E}(u,\, d)(v,\, \beta) = \int_0^L \left(E(d)\, u'v' + \left(\frac{1}{2} E'(d)\, u'^2 + \frac{\mathcal{G}_c}{c_\omega} \frac{\omega'(d)}{\ell} \right) \beta + \frac{2\mathcal{G}_c}{c_\omega} \ell d'\beta' \right) \mathrm{d}x \tag{23a}$$

$$d\mathcal{E}^2(u,\, d)(v,\, \beta) = \int_0^L \left(E(d)\, v'^2 + 2E'(d)\, u'v'\beta + \left(\frac{1}{2} E''(d)\, u'^2 + \frac{\mathcal{G}_c}{c_\omega} \frac{\omega''(d)}{\ell} \right) \beta^2 + \frac{2\mathcal{G}_c}{c_\omega} \ell \beta'^2 \right) \mathrm{d}x \tag{23b}$$

Since at the onset of instability the bar is still in a homogeneous state, and considering Equation (20a), we can rephrase Equation (23) as:

$$d\mathcal{E}(u,\, d)(v,\, \beta) = \int_0^L \left(\frac{1}{2} E'(d)\, u'^2 + \frac{\mathcal{G}_c}{c_\omega} \frac{\omega'(d)}{\ell} \beta \right) \mathrm{d}x \tag{24a}$$

$$d\mathcal{E}^2(u,\, d)(v,\, \beta) = \int_0^L \left(E(d)\, v'^2 + 2E'(d)\, tv'\beta + \left(\frac{1}{2} E''(d)\, t^2 + \frac{\mathcal{G}_c}{c_\omega} \frac{\omega''(d)}{\ell} \right) \beta^2 + \frac{2\mathcal{G}_c}{c_\omega} \ell \beta'^2 \right) \mathrm{d}x \tag{24b}$$

For the elastic phase, the state is stable due to the positiveness of the first derivative for all $\beta \neq 0$. In the damage phase $U_t \geq U_e$, the first derivative, Equation (24a), will vanish considering Equation (22). To check stability, we must consider of the second derivative, Equation (24b), for positiveness. Equation (24b) is therefore rewritten as:

$$d\mathcal{E}^2(u,\, d)(v,\, \beta) = \int_0^L \frac{2\mathcal{G}_c}{c_\omega}\ell\beta'^2 \mathrm{d}x + \int_0^L E(d)\left(v' + \frac{E'(d)}{E(d)}t\beta\right)^2 \mathrm{d}x - \int_0^L \left(\frac{1}{2}S''(d)\sigma_t^2 - \frac{\mathcal{G}_c}{c_\omega}\frac{\omega''(d)}{\ell}\right)\beta^2 \mathrm{d}x \tag{25}$$

Due to the stress softening assumption, Equation (6d), the last term in Equation (25) is negative and can produce a negative second-order derivative. To study the sign of the second-order derivative we consider the Rayleigh quotient:

$$\mathcal{R}_t(v,\beta) = \frac{\int_0^L \frac{2\mathcal{G}_c}{c_\omega}\ell\beta'^2 \mathrm{d}x + \int_0^L E(d)\left(v' + \frac{E'(d)}{E(d)}t\beta\right)^2 \mathrm{d}x}{\int_0^L \left(\frac{1}{2}S''(d)\sigma_t^2 - \frac{\mathcal{G}_c}{c_\omega}\frac{\omega''(d)}{\ell}\right)\beta^2 \mathrm{d}x} \tag{26}$$

with $\sigma_t = E(d)u' = E(d)t$. A sufficient (resp. necessary) condition for stability is then:

$$\rho(u,d) = \min_{(v,\beta)\in(C_0,\mathcal{P})} \mathcal{R}_t(v,\beta) > (\text{resp. } \geq)\ 1 \tag{27}$$

which yields the infimum of the Rayleigh quotient, Equation (26):

$$\rho = \frac{1}{\psi}\begin{cases} E(d)S'(d)^2\sigma_t^2 & \text{else} \\ \left(2\pi^2\frac{\mathcal{G}_c}{c_\omega\ell}\frac{\ell^2}{L^2}E(d)^2S'(d)^4\sigma_t^4\right)^{1/3} & \forall d_t'(0) = 0\ \&\ \forall d_t'(L) = 0\ \&\ \left(2\pi^2\frac{\mathcal{G}_c\ell}{c_\omega} < E(d)S'(d)^2\sigma_t^2L^2\right) \end{cases} \tag{28}$$

with $\psi = \frac{1}{2}S''(d)\sigma_t^2 - \frac{\mathcal{G}_c}{c_\omega}\frac{\omega''(d)}{\ell}$. $d_t'(0)$ and $d_t'(L)$ are from the homogeneous and the non-homogeneous solution space. $d_t'(0) = 0$ represents all possible-phase field solutions which are equal to zero at $x = 0$. The same definition applies to $d_t'(L)$. Here, we give the infimum ρ of $\mathcal{R}_t(v,\beta)$ as a piecewise function, which is different from that one provided in [39, 41]. This is because for a certain choice of $\omega(d)$, the boundary conditions at $x = 0$ and $x = L$ of the phase-field variable d cannot be always guaranteed, which can lead to a solution different from that given in [39].

To elaborate the issue of stability, we consider the phase-field models provided in Table 1.

Phase field model AT1: $a(d) = (1-d)^2$ and $\omega(d) = d$.
The boundary conditions $d_t'(0) = 0$ and $d_t'(L) = 0$ are always satisfied in the case of either homogeneous or non-homogeneous state [19]. Thus, we can obtain the infimum of the Rayleigh quotient as:

$$\rho^3 = \frac{32\pi^2}{27}\left(\frac{\ell}{L}\right)^2\left(\frac{U_e}{U_t}\right)^2 \qquad U_e = \frac{L}{E_0}\sqrt{\frac{\mathcal{G}_cE_0}{c_\omega\ell}} \tag{29}$$

with U_e the displacement at the elastic limit, and U_t the displacement at $x = L$ for $U_t \geq U_e$. From this identity, we deduce that the homogeneous state of the bar is stable if and only if the length of the bar satisfies:

$$\frac{L}{\ell} \leq \chi_c\frac{U_e}{U_t} \qquad \chi_c = \frac{4\sqrt{2}\pi}{3\sqrt{3}} \tag{30}$$

Please note that the expression for χ_c is slightly different from that given in [39] since the coefficient ratio in the surface energy function, Equation (5) is different.

Dependeing on the length of the bar, L, we have two different conditions:

- when $L \geq \chi_c\ell$, the homogeneous state is not stable for any $U_t \geq U_e$. A localisation will arise after the elastic phase.
- when $L < \chi_c\ell$, the homogeneous state is still stable for a finite interval $[U_e, \chi_cU_e\ell/L)$. The onset of instability is then for $U_t \geq \chi_cU_e\ell/L$.

Phase field model AT2: $a(d) = (1-d)^2$ and $\omega(d) = d^2$.
The boundary condition $d_t'(0) = 0$ and $d_t'(L) = 0$ are now satisfied only for homogeneous deformations. For inhomogeneous deformations, the boundary conditions read $d_t'(0) \neq 0$ and $d_t'(L) \neq 0$ [17], and we must use the first expression in Equation (28) to evaluate the infimum of the Rayleigh ratio:

$$\rho = \frac{1}{\psi} E(d) S'(d)^2 \sigma_t^2 = \frac{4}{3} \frac{U_t^2}{U_t^2 - U_e^2} > 1 \tag{31}$$

which indicates that the bar is always deforming homogeneously, irrespective of the bar length. This contrasts with the analysis of Pham [39] and Marigo [44]. It is noted that the boundary conditions $d_t'(0) = 0$ and $d_t'(L) = 0$ are not necessarily satisfied for inhomogeneous deformation, which is unlike the assumption in [39, 44]. However, $d_t(0) = 0$ and $d_t(L) = 0$ could have been enforced artificially in order to obtain a non-homogeneous solution [17, 39].

Phase field model PCM: For this case, the boundary conditions $d_t'(0) = 0$ and $d_t'(L) = 0$ are always satisfied. The infimum of the Rayleigh quotient reads:

$$\rho^3 = \left(\frac{\ell_{ch}}{L}\right)^2 \left(\frac{U_e}{U_t}\right)^2 \qquad\qquad U_t \geq U_e \tag{32}$$

The homogeneous state of the bar is stable if and only if the length of the bar satisfies:

$$L \leq \ell_{\text{ch}} \frac{U_e}{U_t} \tag{33}$$

which shows that the stability of the bar is length-scale insensitive. It only depends on the characteristic length ℓ_{ch}, which is different from model AT1. Depending on the length of the bar length, there are two different possibilities:

- when $L \geq \ell_{\text{ch}}$, the homogeneous state becomes unstable after $U_t \geq U_e$. A localised solution will occur at the end of the elastic phase.
- when $L < \ell_{\text{ch}}$, all states in the displacement interval $[U_e,\, U_e \ell_{\text{ch}}/L)$ are stable. Unstable solutions occur for $U_t \geq U_e \ell_{\text{ch}}/L$.

4.2. Non-homogeneous solutions, damage profile and irreversibility

If $\rho\,(u, d) \leq 1$, the bar will lose stability, opening up the possibility of a non-homogeneous solution. We will now study the non-homogeneous solution and focus on stress-softening materials with an elastic regime, such as models AT1 and PCM. We assume the homogeneous state to become unstable immediately after the elastic phase, i.e. when $\rho\,(u, 0) \leq 1$, which yield the first lower bound L_b^1 for the bar length L, see Table 2.

We suppose that $\mathcal{S} = (x_0 - D,\, x_0 + D)$ is a localised zone and that $\sigma_t \in (0,\, \sigma_e)$ is the stress in the bar. x_0 and D are the centre and the half bandwidth of the localised zone, respectively. σ_e denotes the elastic limit, and $\sigma_e = f_t$ considering the above assumptions. Outside the localised zone $\mathcal{S}$ the phase field is zero. The damage criterion in Equation (18c) now becomes an equality:

$$\frac{1}{2} E'\,(d)\; u'^2 + \frac{\mathcal{G}_c}{c_\omega \ell} \omega'(d) - \frac{\mathcal{G}_c}{c_\omega} \ell d'' = 0 \quad \text{in} \quad \mathcal{S}; \quad d = 0 \quad \text{in} \quad (0,\, L)\,/\mathcal{S} \tag{34}$$

with the boundary conditions $d\,(x_0 \pm D) = d'\,(x_0 \pm D) = 0$, and can be used to determine the damage profile in $\mathcal{S}$. We can rephrase Equation (34) by multiplication by d' and integration with respect to x:

$$-\sigma_t^2 S\,(d) + \frac{2\mathcal{G}_c}{c_\omega \ell} \omega(d) - \frac{2\mathcal{G}_c}{c_\omega} \ell\,(d')^2 = -\frac{\sigma_t^2}{E_0} \tag{35}$$

with $S\,(d) = 1/E(d)$ and $\sigma_t = E(d) u'$.

At the centre x_0 of the localised zone, the phase field $d(x)$ attains its maximum d_m, while $d'(x_0) = 0$ due to the symmetry of $d(x)$. From Equation (35) we then obtain the stress in the bar:

$$\sigma_t = \sqrt{\frac{2\mathcal{G}_c}{c_\omega \ell}\frac{\omega(d_\mathrm{m})}{S(d_\mathrm{m}) - 1/E_0}} = \sqrt{\frac{2\mathcal{G}_c E_0}{c_\omega \ell}\frac{\omega(d_\mathrm{m})}{E_0/E(d_\mathrm{m}) - 1}} \tag{36}$$

Considering the elastic limit σ_e in Equation (21) and setting $\sigma_e = f_t$ yields

$$f_t = \sqrt{\frac{2\mathcal{G}_c}{c_\omega \ell}\frac{\omega'(0)}{S'(0)}} \qquad \sigma_t = f_t\sqrt{\frac{S'(0)}{\omega'(0)}\frac{\omega(d_\mathrm{m})}{S(d_\mathrm{m}) - 1/E_0}} = f_t\sqrt{\frac{S'(0)}{\omega'(0)}\frac{E_0\omega(d_\mathrm{m})}{E_0/E(d_\mathrm{m}) - 1}} \tag{37}$$

Table 2: Properties of the phase-field models. The regularisation length ℓ, the initial half bandwidth D_0, the final half bandwidth D_u, the lower bound L_b^1 of the bar length (from $\rho(u, 0) \leq 1$ in Equation (28)), the lower bound L_b^2, and the upper bound L_u.

Model	ℓ	D_0	D_u	L_b^1	L_b^2	L_u
AT1	$\frac{3}{8}\ell_\mathrm{ch}$	$\sqrt{\frac{2}{3}}\pi\ell$	2ℓ	$\frac{4}{3}\sqrt{\frac{2}{3}}\pi\ell$	4ℓ	$\sqrt{\frac{2}{3}}\pi\ell_\mathrm{ch}$
AT2	no elastic phase	∞	∞	∞	∞	∞
PCM	independent of ℓ	$\frac{\pi}{2}\ell$	$\frac{\pi}{2}\ell$	ℓ_ch	$\pi\ell$	$2\ell_\mathrm{ch}$

The first expression in Equation (37) gives the restriction on the regularisation length ℓ in order that the elastic limit $\sigma_e = f_t$ can be attained, see Table 2. For model AT2, there is no elastic phase in the response of the bar. Model PCM has an elastic phase, but σ_t is independent of the regularisation length ℓ [21]. Due to ℓ being independent from σ_t, model PCM is probably the best for analysing crack propagation, attaining a proper force-displacement response and obtaining reliable crack patterns for small values of ℓ [21].

Rewriting Equation (35) further gives:

$$\ell^2 (d')^2 = \mathcal{H}(\sigma_t, d), \qquad \text{with} \qquad \mathcal{H}(\sigma_t, d) = \omega(d) - \frac{\sigma_t^2 (E_0 S(d) - 1)}{A_0} \qquad A_0 = 2\frac{\mathcal{G}_c E_0}{c_\omega \ell} \tag{38}$$

Due to the stress-softening assumption, $\mathcal{H}(\sigma_t, d)$ is a decreasing function of σ_t, and $\mathcal{H}(\sigma_t, d) \geq 0$. This gives the half bandwidth of the localisation zone:

$$D(\sigma_t) = \ell \int_0^{d_\mathrm{m}} \frac{\mathrm{d}\beta}{\sqrt{\mathcal{H}(\sigma_t, \beta)}} \tag{39}$$

For $\sigma_t = f_t$ we have for the phase field $d_\mathrm{m} = 0$, which yields the initial half bandwidth of the localised zone [45]:

$$D_0 = D(f_t) = \pi\ell\sqrt{\frac{2S'(0)}{\omega'(0)S''(0) - S'(0)\omega''(0)}} \tag{40}$$

When the stress reaches $\sigma_t = 0$, so that $d_\mathrm{m} = 1$, we obtain the final half bandwidth [45]:

$$D_u = D(0) = \ell \int_0^1 \frac{1}{\sqrt{\omega(\beta)}}\mathrm{d}\beta \tag{41}$$

4.3. Force-displacement diagram and relation to the cohesive-zone model

We now suppose that there are a time-dependent set of localised zones $\mathcal{S}_t = \bigcup_i \mathcal{S}_t^i$ at time $t \geq t_e$. The total width of the localisation zones is $nD(\sigma_t)$, the integer n being the number of half localisation zones. A half localisation zone can be found either bar end $x = 0$ or $x = L$. Considering Equation (19) and $d_t = 0$ outside the localised zone, we obtain the end displacement at $x = L$ as:

$$U_t = \sigma_t \int_0^L S(d_t)\,\mathrm{d}x = \sigma_t\left[S(0)(L - nD(\sigma_t)) + \sum_i \int_{\mathcal{S}_t^i} S(d_t)\,\mathrm{d}x\right] \tag{42}$$

For a half localisation zone $\mathcal{S}_t^i = (x_i - D(\sigma_t)\,,\ x_i)$, the integral $\sigma_t \int_{\mathcal{S}_t^i} S(d_t)\,\mathrm{d}x$ reads:

$$\zeta = \sigma_t \int_{\mathcal{S}_t^i} S(d_t)\,\mathrm{d}x = \sigma_t \ell \int_0^{d_\mathrm{m}} \frac{S(\beta)\,\mathrm{d}\beta}{\sqrt{\mathcal{H}(\sigma_t, \beta)}} \tag{43}$$

while for an inner localisation zone $\mathcal{S}_t^j = \Big(x_j - D(\sigma_t)\,,\ x_j + D(\sigma_t)\Big)$ the integral is given as $\sigma_t \int_{\mathcal{S}_t^j} S(d_t)\,\mathrm{d}x = 2\zeta$ due to the symmetry of the damage profile.

Considering only inner localisation zones, Equation (42) can be rewritten as:

$$U_t = U_t^e + U_t^j = \frac{\sigma_t L}{E_0} + \frac{\sigma_t}{E_0} \cdot n \cdot 2\ell \int_0^{d_\mathrm{m}} \left(\frac{E_0}{E(\beta)} - 1\right) \frac{\mathrm{d}\beta}{\sqrt{\mathcal{H}(\sigma_t, \beta)}} \tag{44}$$

The first term U_t^e denotes an displacement due to an elastic process, while the second term U_t^j is due to inelasticity in the localisation zones. Since we consider a unit area, Equation (44) also implicitly defines the force-displacement relation of the bar.

The second term U_t^j contributes an additional displacement after the elastic phase. It can be viewed as a displacement jump across the localised zones, since U_t^j is zero in the absence of localisation. Indeed, U_t^j has the physical meaning of the crack separation δ in the cohesive-zone model, and the stress σ_t denotes the traction t acting on the bar cross-section. From Equation (44), we obtain the force-displacement jump relation $(\sigma_t - U_t^j)$ relation, which is identical to the traction-separation $(\sigma - \delta)$ relation when considering a single inner localisation zone:

$$\delta = \frac{\sigma}{E_0} \cdot 2\ell \int_0^{d_\mathrm{m}} \left(\frac{E_0}{E(\beta)} - 1\right) \frac{\mathrm{d}\beta}{\sqrt{\mathcal{H}(\sigma_t, \beta)}} \tag{45}$$

where the term δ denotes the displacement jump across the localisation zone. σ is now identical to the traction t on the cross-section, and the subscript t has been dropped for brevity. The ultimate crack separation or displacement jump equals $\delta_c = \lim_{d_\mathrm{m} \to 1} \delta$.

So far, we have constructed the cohesive-zone model in a 1D setting. Now, we will show that the phase-field method can build the response of Barenblatt's version of the cohesive-zone model, but not Dugdale's variant. For Dugdale's model, Equations (37) and (38) result in:

$$\begin{aligned} \sigma_t = f_t = \text{constant} \quad &\Longrightarrow \quad f_t \sqrt{\frac{S'(0)}{\omega'(0)} \frac{\omega(d)}{S(d) - 1/E_0}} = \text{constant} \\ \Longrightarrow \quad \mathcal{H}(\sigma_t, d) = 0 \quad &\Longrightarrow \quad \ell^2 (d')^2 = 0 \quad \Longrightarrow \quad d = \text{constant} \end{aligned} \tag{46}$$

However, $d = \text{constant}$ contradicts the assumption that the bar is locally damaged and thus has a zone of localised deformations. Therefore, a phase-field method cannot reproduce the response of Dugdale's cohesive-zone model. Obviously, the phase-field method can reproduce Barenblatt's cohesive zone model due to stress softening.

We take model PCM to illustrate the above. Some results has been given before [21, 42], and we will only present the main findings and new aspects:

$$d_\mathrm{m} = 1 - \sigma / f_t\ , \qquad d(\sigma, x) = 1 - \sqrt{1 - \left(2 d_\mathrm{m} - d_\mathrm{m}^2\right) \cos^2 \frac{x}{\ell}}\ , \qquad D(\sigma) = \frac{\pi}{2} \ell \tag{47}$$

Substituting this result into Equation (45) yields the traction-separation relation:

$$\sigma(\delta) = f_t \left(1 - \frac{f_t}{2\mathcal{G}_c} \delta\right), \qquad \delta_c = \frac{2\mathcal{G}_c}{f_t}, \tag{48}$$

which represents the linear cohesive traction-separation law given in Equation (3). The bar will exhibit softening in the process of crack propagation, not a brittle behaviour, which is different from [21].

Substituting Equations (47) and (48) into Equation (5) leads to the energy dissipation during crack propagation:

$$\mathcal{G}(\delta) = \frac{\mathcal{G}_c}{c_\omega}\int_\Omega \left(\frac{\omega(d)}{\ell} + \ell\|\nabla d\|^2\right) \mathrm{d}\Omega = \frac{f_t}{2}\delta = \mathcal{G}_c \frac{U_t/U_e - 1}{2\ell_{\mathrm{ch}}/L - 1} \tag{49}$$

with U_t the end displacement at t and $U_e = f_t L/E_0$. Obviously, the dissipated energy $\mathcal{G}(\delta)$ has a linear relation with the crack separation δ, which is different from that provided in Equation (3). It has the shape of the dissipated energy $\mathcal{G}(\delta)$ given in the Dugdale's cohesive zone model (Equation (2)) with a reduced fracture strength $f_t/2$. It is noted that the expression for $\mathcal{G}(\delta)$ is different from [42].

In sum, the phase field method can partially produce the response of cohesive zone model, including the traction-separation law, but not entirely reproduce the cohesive response, which for instance holds for the dissipated energy. The derived model possesses some properties of Barenblatt's version of the cohesive-zone model, but also some of the Dugdale cohesive-zone model. For the construction of a phase-field regularised cohesive-zone model, the following aspects should be satisfied:

1. The constitutive assumptions in Equation (6) to enforce a stress softening response in the damage phase;
2. The stress evolution, Equation (37), must enforce a stress condition: $\sigma_e = f_t$ (f_t being the fracture strength);
3. The force-displacement or traction-separation ($\sigma - \delta$) relation in Equation (45) must control the $\sigma - \delta$ curve, e.g. a linear or an exponential shape;
4. The ultimate value for the crack separation, $\delta_c = \lim_{d_{\mathrm{m}}\to 1}\delta$ in Equation (45) must equal the ultimate crack separation in the cohesive-zone model.

4.4. Size effects and snapback behaviour

The construction of non-homogeneous solutions is only valid provided that the bar is sufficiently long for a localisation zone to emerge and to grow inside the bar. Thus, we obtain a second lower bound for the bar length L:

$$L \geq L_b^2 = 2D_u = 2\ell\int_0^1 \frac{1}{\sqrt{\omega(\beta)}}\mathrm{d}\beta \tag{50}$$

For the phase field models in Table 1, the lower bound L_b^2 is listed in Table 2. For model AT2 model, the half bandwidth is $D = \infty$, which indicates that the damage spreads over the entire bar. Correspondingly, the boundary conditions $d_t'(0) = 0$ and $d_t'(L) = 0$ can only be satisfied in the case of homogeneous deformations. Indeed, the homogeneous solution is the only solution in the damage phase, cf. Equation (31). Combining L_b^1 and L_b^2 gives the lower bound for L at which a non-homogeneous solution can emerge:

$$L_b = \max\left(L_b^1,\, L_b^2\right) \tag{51}$$

We consider the case $L \geq L_b$. The initial slope of the force-displacement curve which is related to n localised zones, is then given by (after $t > t_e$):

$$\frac{\mathrm{d}U_t}{\mathrm{d}\sigma} = \frac{L}{E_0} + n\frac{\mathrm{d}\delta}{\mathrm{d}\sigma} \qquad \sigma \in [0,\, f_t] \tag{52}$$

To avoid snapback behaviour in the force-displacement curve, we consider the following relation, which yields an upper bound for the bar length L:

$$\frac{\mathrm{d}U_t}{\mathrm{d}\sigma} < 0 \quad \Longrightarrow \quad L \leq n\cdot L_u^i = n\cdot\inf\left\{-E_0\frac{\mathrm{d}\delta}{\mathrm{d}\sigma}\right\} \qquad \text{with} \qquad \sigma \in [0,\, f_t] \tag{53}$$

If we consider only one inner localisation zone, $n = 1$, it follows from Equation (53) that:

$$L_u = -E_0\left.\frac{\mathrm{d}\delta}{\mathrm{d}\sigma}\right|_{\sigma=f_t} = \frac{4\omega'(0)^2}{\pi^2 c_\omega}\ell_{ch}\left(\frac{D_0}{\ell}\right)^3 \tag{54}$$

to avoid snapback behaviour after $t = t_e$. For the phase-field models of Table 1, the upper bounds for L are given in Table 2. For model AT2, the upper bound of L is infinite and the force-displacement curve will not exhibit snapback.

When we only consider inner localisation zones, three different responses can occur:

- when $L \leq \min\left(L_b^1, L_b^2\right)$, no localisation zone will appear at the end of the elastic phase $t = t_e$, and the homogeneous response is the only solution;
- when $L_b < L \leq L_u$, localisation will happen inside the bar, but the force-displacement curve will not exhibit snapback behaviour after $t = t_e$;
- when $L > L_u$, the force-displacement curve will present a snapback at the end of the elastic phase, i.e. after $t = t_e$, and localisation zones appear inside the bar. Due to the localisation, some parts of the bar elongate or are loaded while the other parts contract or unload, see Figure 2(a).

4.5. Crack nucleation inside the bar

We now study crack nucleation inside the 1D bar and show that the phase-field models in Table 1 can reconcile the energy and stress criteria, and account for scale effects. Different from [46], we identify the crack nucleation with a fully localised solution such that $\max_{x\in(0,\,L]} d\,(x) = 1$ instead of an energy jump, because there may be no such a sudden jump of the elastic and the surface energy (see Figure 8(b)). We assume that the crack nucleates right after $t = t_c$, the time just before which the phase field takes its maximum value $d_{\mathrm{m}} < 1$ ($t = t_c^-$), and right after which the phase field is $d_{\mathrm{m}} = 1$ ($t = t_c^+$). The necessary conditions for crack initation are:

$$\text{Energy criterion:} \qquad -\frac{\partial W_p}{\partial A} = \mathcal{G} \geq \mathcal{G}_c, \tag{55a}$$

$$\text{Stress criterion:} \qquad \sigma_c \geq f_t \tag{55b}$$

with W_p being the potential energy, A being the surface. $\mathcal{G}$ denotes the fracture energy per unit surface and σ_c is the critical stress at $t = t_c$.

For model AT1, crack nucleation occurs when a critical stress, $\sigma_c = O\left(\sqrt{\mathcal{G}_c E_0/\ell}\right)$ is attained [46], provided that the bar length $L \geq L_u$. If the regularisation length ℓ is identified in Table 2, the critical stress reads $\sigma_c = f_t$. Obviously, the stress criterion (55b) is fulfilled. When $L \geq L_u$ the force-displacement curve will exhibit a snapback and the energy balance may not be satisfied. The unbalanced energy will convert to other types of energy, e.g., kinematic energy. Consequently, the energy criterion (55a) is enforced automatically [47].

If $L_b \leq L < L_u$, the bar will lose stability right after the elastic phase $t = t_e$. The bar will experience a strain-softening phase, in which the stress criterion (55b) is not guaranteed. After this phase, the bar will be fully broken. However, the energy criterion always holds. An equivalent critical stress σ_c^{eq} has been proposed for crack nucleation just after an elastic phase [46], $\sigma_c^{\mathrm{eq}} = \sqrt{2\mathcal{G}_c/E_0 L}$. If we substitute σ_c^{eq} in Equation (55b), the stress criterion can be satisfied.

For model PCM, σ_t is independent of the regularisation length ℓ and we can adopt a small value for ℓ to accurately resolve the crack path. Accordingly, the lower bound of the bar length in Table 2 is given by $L_b = \ell_{\mathrm{ch}}$. When $L/L_b = L/\ell_{\mathrm{ch}} \geq 1$, localisation will appear inside the bar at the end of elastic phase $t = t_e$. Similar to model AT1, crack nucleation is governed by the bar length. If $1 \leq L/\ell_{\mathrm{ch}} \leq 2$ the bar loses stability and will exhibit localised deformations, but this will not result in a snapback. Also similar to model AT1, the necessary conditions for a crack nucleation in Equation (55) are confirmed with an equivalent critical stress $\sigma_c^{\mathrm{eq}} = \sqrt{2\mathcal{G}_c/E_0 L}$, see the dotted curve in Figure 2(b). When $L/\ell_{\mathrm{ch}} \geq 2$, localised deformations will also occur, but in addition there will be a snapback. The stress and energy criterion are guaranteed like for model AT1, shown as the solid curve in Figure 2(b).

5. Finite element implementation

Equation (13) can either be solved in a monolithic way [27] or in a staggered form [17]. Hierein, we will employ a monolithic approach with an arc-length control for the solution of the coupled, nonlinear problem given in Equations (13)-(14). The arc-length control is based on the rate of the internal and the dissipated energy [48], defined as:

$$\text{Rate of the internal energy:} \qquad \frac{1}{2}\left(\lambda_{i+1}\mathbf{u}_{i+1}^{\mathrm{T}} - \lambda_i \mathbf{u}_i^{\mathrm{T}}\right)\cdot\bar{\mathbf{f}} - \Delta\tau^U = 0, \tag{56a}$$

$$\text{Rate of the dissipated energy:} \qquad \frac{1}{2}\left(\lambda_i\mathbf{u}_{i+1}^{\mathrm{T}} - \lambda_{i+1} \mathbf{u}_i^{\mathrm{T}}\right)\cdot\bar{\mathbf{f}} - \Delta\tau^D = 0, \tag{56b}$$

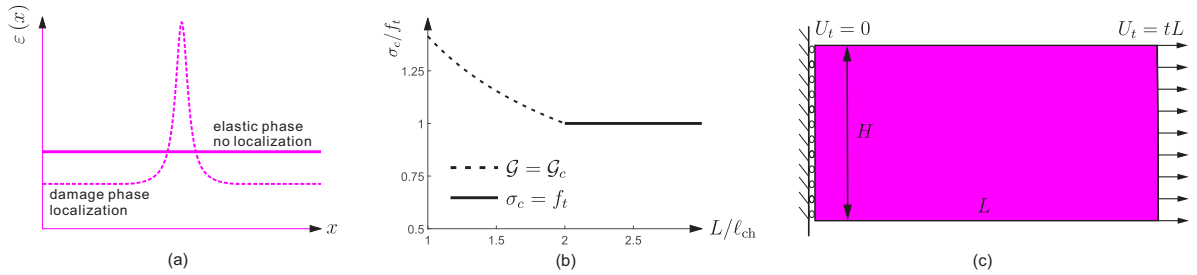

Figure 2: (a) Strain distribution before and after localisation, (b) Normalised stress σ_c/f_t at crack nucleation for the bar, (c) Uniaxial traction of a bar with an imposed end-displacement.

with λ the loading parameter, and $\mathbf{u}_i$ being the displacement field at the time step i. $\bar{\mathbf{f}}$ denotes a normalised load vector, $\Delta\tau^U$ represents the prescribed amount of the internal energy, and $\Delta\tau^D$ is the prescribed amount of energy which needs to be dissipated. For the AT1 and PCM models, there is a linear elastic phase before $t = t_e$. In the elastic phase the rate of the internal energy in Equation (56a) is used as the arc-length function. Different from [48], however, we take the resultant force F_t at the end of the bar to indicate the switch to using the rate of energy dissipation as the arc-length parameter. It is noted that $F_t = \sigma_t \leq \sigma_e$, σ_e being the elastic stress limit in Equation (21). If $|F_t - \sigma_e|/\sigma_e < \text{tol}$ we switch from the internal energy to the dissipated energy as control parameter, with $\text{tol} = 10^{-6}$ in the examples of Section 6,

To enforce the irreversibility condition $\dot{d} \geq 0$ in Equation (14a), a penalty term is added in (5) [17, 49]:

$$E_p(d) = \frac{\lambda}{2}\int_\Omega \langle d - d_i\rangle_-^2 \, \mathrm{d}\Omega \quad \text{with} \quad \lambda \gg \frac{\mathcal{G}_c}{c_\omega}\frac{1}{\ell} \tag{57}$$

which implies $d \geqslant d_i$; d_i denote phase field values from the previous step. To maintain well-posedness for a partially broken domain, a small parameter η has been added in the expression for the degradation function, $a(d) + \eta$ [17], with $\eta = 10^{-5}$ in this study.

Herein, we exploit C^1-continuous Powell-Sabin B-splines for the spatial discretisation [25, 50–52]. A flexible control of the geometry is possible, such as remeshing using any standard package for triangular elements [53], while the C^1-continuity assures an improved stress prediction. Powell-Sabin B-splines describe the geometry and interpolate the displacement field $\mathbf{u}$ and the phase field d in an isoparametric sense:

$$\mathbf{x} = \sum_{k=1}^{N_v}\sum_{j=1}^{3} N_k^j \boldsymbol{X}_k^j \qquad \mathbf{u} = \sum_{k=1}^{N_v}\sum_{j=1}^{3} N_k^j \boldsymbol{U}_k^j \qquad d = \sum_{k=1}^{N_v}\sum_{j=1}^{3} N_k^j d_k^j \tag{58}$$

where $\boldsymbol{X}_k^j$ represent the coordinates of the corners $\boldsymbol{Q}_k^j$ of the Powell-Sabin triangles, $\boldsymbol{U}_k^j$ and d_k^j denote the degrees of freedom at $\boldsymbol{Q}_k^j$, and N_v is the total number of vertices. The indices $j = 1, 2, 3$ imply that three Powell-Sabin B-splines are defined on each vertex k. Three Powell-Sabin B-splines N_k^j are defined on each vertex k.

6. Numerical examples

We now demonstrate the performance of the methodology to construct the cohesive response by the phase field method through some representative simulations. We present examples with stress-softening materials, and with crack propagation in a square plate. In the example, a two-dimensional version of a uniaxial tension example is revisited to study the homogeneous and non-homogeneous solutions of a 1D bar [39]. The stability and the snapback behaviour of the bar will be addressed. The computed force-displacement diagrams and the energy evolution will be given. Moreover, we will illustrate the construction of the cohesive-zone model by the phase-field methodology in a 1D setting.

We consider a rectangular domain under tension. Figure 2(c) shows the geometry and the boundary conditions. With a suitable rescaling of the loading, we can set Young's modulus $E_0 = 10$, the fracture strength $f_t = 1$ and the

surface energy $\mathcal{G}_c = 1$ in the numerical experiments. Poisson's ratio is set $\nu = 0.0$. A unit cross-sectional area is considered with a height $H = 1$. The phase-field models in Table 1 are used to study the stability and snapback behaviour of the bar. Analytical and numerical results are presented. The analytical results are obtained directly from the corresponding formulations if a closed-form solution is available, otherwise by numerical integration on basis of the analytical expressions. As detailed in Section 4.4, model AT2 does not lose stability and neither displays snapback behaviour. Thus, the homogeneous solution is unique. The other two phase-field models in Table 1 may lose stability and exhibit snapback behaviour, depending on the length of the bar.

For the homogeneous solution, the stress σ_t, the phase field d_t, and the elastic and surface energies are obtained from Equations (22) and (17). In the non-homogeneous state, we can obtain the stress σ_t and the end displacement U_t at t from Equations (36) and Equation (44), respectively. The elastic and surface energies are given by Equation (17). The maximum phase field d_{m} is computed with the aid of Equation (36). The displacement jump δ and the ultimate displacement jump δ_c are given by Equation (45). In the analysis, we only consider the case of the localisation zone inside the bar. The precise location of the localisation zone is energetically irrelevant. It may vary depending on numerical errors [39].

6.1. Phase field model AT1

The degradation function reads $a(d) = (1 - d)^2$ and the homogeneous energy dissipation function is given by $\omega(d) = d$. According to Equation (21), this phase-field model has a non-vanishing elastic regime with a yield stress $\sigma_e = f_t$ if we choose the regularisation length ℓ as in Table 2. In Section 4.4, we have discussed the size effect of the bar length analytically. Now, we will study the size effect numerically. Three situations can occur, depending on the length of the bar. To capture the snapback response of the plate, the monolithic approach with an arc-length control is used in the solution scheme.

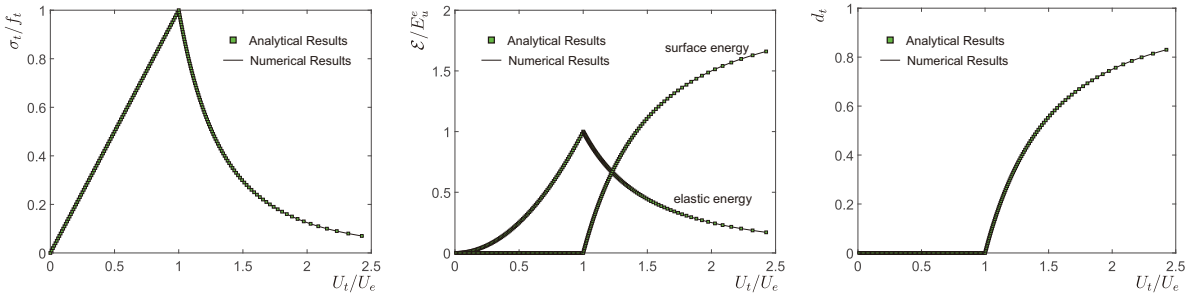

Figure 3: Load-displacement response (σ_t–U_t), evolution of elastic and surface energies ($\mathcal{E}$–U_t) and phase field-displacement relation (d_t–U_t). f_t and U_e denote the elastic stress limit and the displacement limit in Equation (21), respectively.

Case 1: bar length $L = 5 < \min\left(L_b^1, L_b^2\right)$. The bar now does not lose stability. The homogeneous solution is unique, cf. Equations (21) and (22). For the elastic phase, $t \leq t_e$, it can be obtained in a straightforward manner (not presented here). For $t > t_e$ the homogeneous solution is given by:

$$\frac{\sigma_t}{f_t} = \left(\frac{U_e}{U_t}\right)^3 \qquad d_t = 1 - \left(\frac{U_e}{U_t}\right)^2 \qquad \frac{E_u^t}{E_u^e} = \left(\frac{U_e}{U_t}\right)^2 \qquad \frac{E_s^t}{E_u^e} = 2\left(1 - \left(\frac{U_e}{U_t}\right)^2\right) \tag{59}$$

with σ_t, d_t, E_u^t and E_s^t being the stress, the phase field, the elastic energy and the surface energy at current time t, respectively. f_t is the fracture strength, E_u^e is the elastic energy limit at t_e, while $E_u^e = E_0 U_e^2/2L$, U_t and U_e denote the end displacement at $x = L$, $U_e = f_t L/E_0$, respectively.

Figure 3 shows the comparison between the numerical and analytical solutions. A good agreement is obtained. An elastic phase is clearly observed when $U_t \leq U_e$. After $U_t = U_e$, the bar will start to be damaged with a non-zero surface energy and a phase field d. In a homogeneous state, the phase field is uniform in the plate, not shown here.

Case 2: bar length $\max\left(L_b^1, L_b^2\right) < L = 20 < L_u$. A non-homogeneous solution is now obtained after $t = t_e$, but closed-form solutions are not available, so the analytical expressions are integrated numerically. The bar does not exhibit snapback behaviour directly after $t = t_e$, see the force-displacement diagram in Figure 4(a). Figure 4 presents

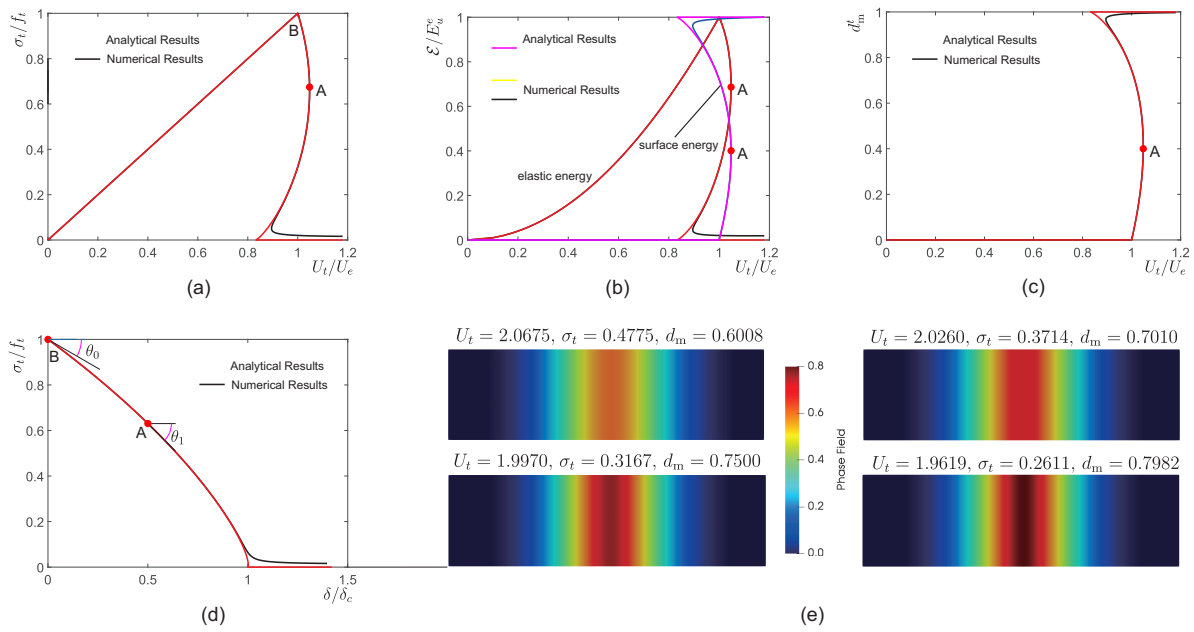

Figure 4: (a) Load-displacement response (σ_t–U_t), (b) Evolution of the elastic and surface energies ($\mathcal{E}$–U_t), (c) Phase field-displacement relation ($d^t_{\rm m}$–U_t), (d) Stress-displacement jump (separation) relation, (e) Contour plot of the phase field d at different load steps. $d^t_{\rm m}$ is the maximum phase field along the plate at t, $U_e = f_t L/E_0$ is the limit of the 'elastic' limit in Equation (21), $E^e_u = E_0 U_e^2/2L$ is the limit of the elastic energy at t_e, δ and $\delta_c = 3\sqrt{2\pi\mathcal{G}_c}/8f_t$ denote the displacement jump and the ultimate displacement jump in Equation (45), respectively.

plots of the force-displacement relation, the energy and the phase field during damage evolution. The numerical results well match the analytical results, which validate the numerical implementation in Section 5. When the phase field value d approaches $d = 1$ (broken state), the tails of each figure show some discrepancy due to the influence of the regularisation length ℓ and the introduction of η in the degradation function $a(d)$ in Equation (5).

According to Equation (37), the bar will experience damage evolution after $t = t_e$. There is structural strain softening from points B to A in Figure 4(a). Thereafter, the diagrams of the force-displacement (Figure 4(a)), the energy (Figure 4(b)) and the phase field (Figure 4(c)) show a snapback since:

$$|\theta_0| < |\theta_1| \quad \Longrightarrow \quad \left.\frac{\mathrm{d}\delta}{\mathrm{d}\sigma}\right|_A > \left.\frac{\mathrm{d}\delta}{\mathrm{d}\sigma}\right|_B \quad \Longrightarrow \quad -E_0 \left.\frac{\mathrm{d}\delta}{\mathrm{d}\sigma}\right|_A < -E_0 \left.\frac{\mathrm{d}\delta}{\mathrm{d}\sigma}\right|_B \tag{60}$$

with θ_0 and θ_1 being the angles of the tangent line at point B and A, respectively. From Equation (53), we obtain $L^A_u < L = 20 < L^B_u$, which indicates that the upper bound of the bar length L at point B is larger than that at A. While the displacement U_t and the stress σ_t then become smaller, the phase field (the damage) continues to evolve, see Figure 4(e). Figure 4(d) shows the traction-separation curve in the cohesive-zone model. While the phase-field model of Equation (6.1) has been designed for the simulation of brittle fracture [19], it has the character of a cohesive-zone model for a proper choice of the regularisation length ℓ, see Table 2. Such a cohesive response has also been observed in the analysis of an L-shaped beam subject to a vertical load [54].

Case 3: bar length $L_u < L = 27.5$. The bar will now lose stability and exhibit snapback behaviour right after $t = t_e$. Figure 5 presents the load-displacement response, and the evolution of the energy and the phase field. The figure shows that the numerical simulations well capture the behaviour of the bar. Similar to Figure 4, the tails in Figure 5 show some discrepancy. In Figure 5(a), the angle of the tangent line at B ($t = t_e$) is $0 < \theta_0 < \pi/2$, which results a snapback right after this point. This also holds for the evolution of the energy and the phase field evolution, Figures 5(b)/(c). In Figure 5(b) the maximum elastic energy E_u is different from the maximum surface energy E_s. The stress criterion (55b) yields the critical stress $\sigma_c = f_t$ at $t = t_e$, see Figure 5(a).

Figure 5(e) shows the contour plots of the phase field. Due to the snapback, the displacement U_t and the stress σ_t become smaller, but the phase field continues to evolve. Due to the localisation the displacement U_t is composed of two parts: the elastic displacement and the displacement jump δ associated with the localisation zone, see Equation

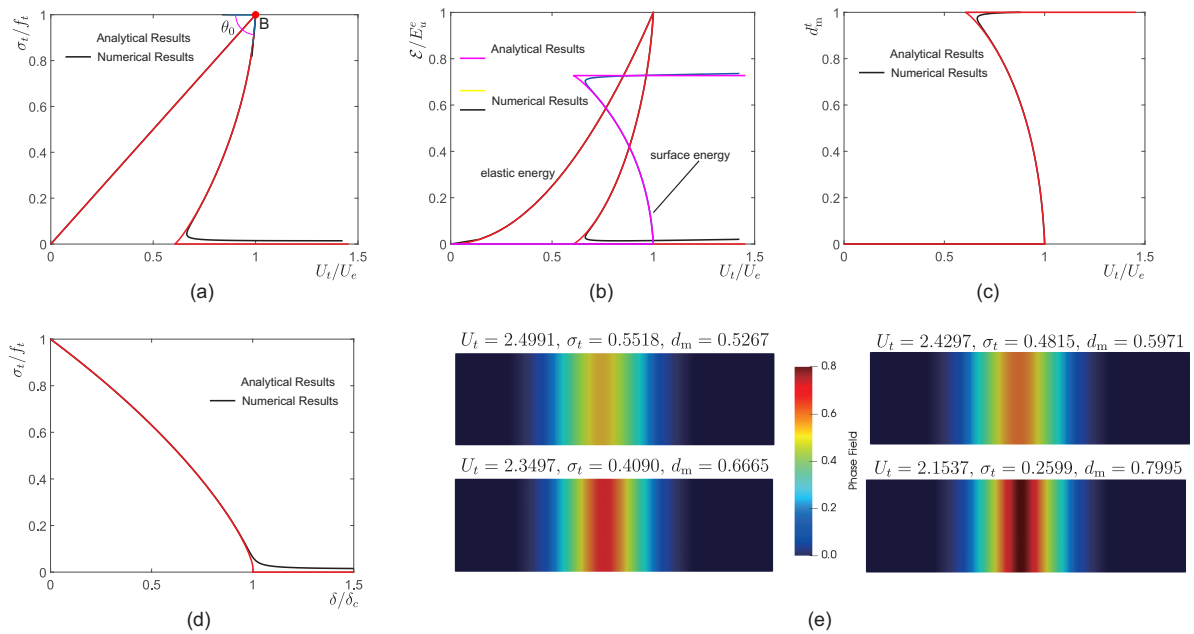

Figure 5: (a) Load-displacement response (σ_t–U_t), (b) Evolution of the elastic and surface energies ($\mathcal{E}$–U_t), (c) Phase field-displacement relation (d_{m}^t–U_t), (d) Stress-displacement separation relation, (e) Contour plots of the phase field d for different load steps. d_{m}^t is the maximum phase field along the plate at time step t, $U_e = f_t L/E_0$ is the limit of the 'elastic' in Equation (21), $E_u^e = E_0 U_e^2/2L$ is the limit of the elastic energy limit at time step t_e.

(44). In Equation (45) δ is independent of the bar length L. Thus, Figure 5(d) presents an identical stress-displacement separation curve as in Figure 4(d).

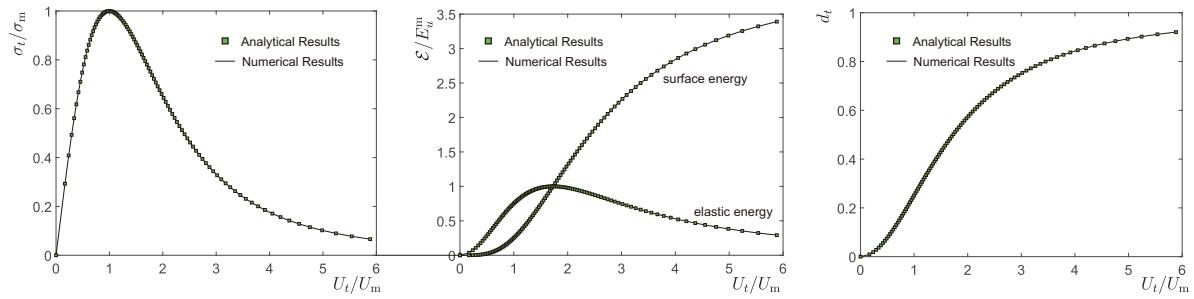

Figure 6: Load-displacement response (σ_t–U_t), evolution of elastic and surface energies ($\mathcal{E}$–U_t) and phase field-displacement relation (d–U_t). Here, σ_{m} and U_{m} denote the maximum stress and the displacement, respectively, obtained from Equation (22). The bar length is $L = 5$.

6.2. *Phase field model* AT2

The bar will now continue to deform homogeneously throughout the loading process, independent of the bar length, see also Section 4.1. The homogeneous solution is unique:

$$\frac{\sigma_t}{\sigma_{\mathrm{m}}} = \frac{16\,(U_t/U_{\mathrm{m}})}{\left((U_t/U_{\mathrm{m}})^2+3\right)^2} \qquad d_t = \frac{(U_t/U_{\mathrm{m}})^2}{(U_t/U_{\mathrm{m}})^2+3} \qquad \frac{E_u^t}{E_u^{\mathrm{m}}} = \frac{16\,(U_t/U_{\mathrm{m}})^2}{\left((U_t/U_{\mathrm{m}})^2+3\right)^2} \qquad \frac{E_s^t}{E_u^{\mathrm{m}}} = \frac{16}{3}\frac{(U_t/U_{\mathrm{m}})^4}{\left((U_t/U_{\mathrm{m}})^2+3\right)^2} \tag{61}$$

with σ_{m}, U_{m} and E_u^{m} being the maximum stress, the corresponding displacement, and the strain energy, respectively:

$$\sigma_{\mathrm{m}} = \frac{3\sqrt{3}}{8\sqrt{2}}\sqrt{\frac{\mathcal{G}_c E_0}{c_\omega \ell}} \qquad U_{\mathrm{m}} = \frac{16\sigma_{\mathrm{m}} L}{9E_0} \qquad E_u^{\mathrm{m}} = \frac{8\sigma_{\mathrm{m}}^2 L}{9E_0} \tag{62}$$

We have tested several values for L and obtained homogeneous results throughout (not shown for conciseness). Figure 6 shows the load-displacement curve, and the evolution of the energy and the phase field, with the numerical results matching the analytical values. There is no elastic phase in the evolution process because the bar is damaged from the onset with a non-zero surface energy and phase field d. During damage evolution, the stress and the elastic energy are maximised, which is consistent with Equation (22).

6.3. Phase field model PCM

This phase field model has a non-vanishing elastic phase with a yield stress f_t. For $t \geq t_e$, the bar will be damaged. Then, there are three solutions, depending on the length of the bar L. To capture the snapback behaviour, a monolithic arc-length control scheme has been used. The regularisation length $\ell = 4$.

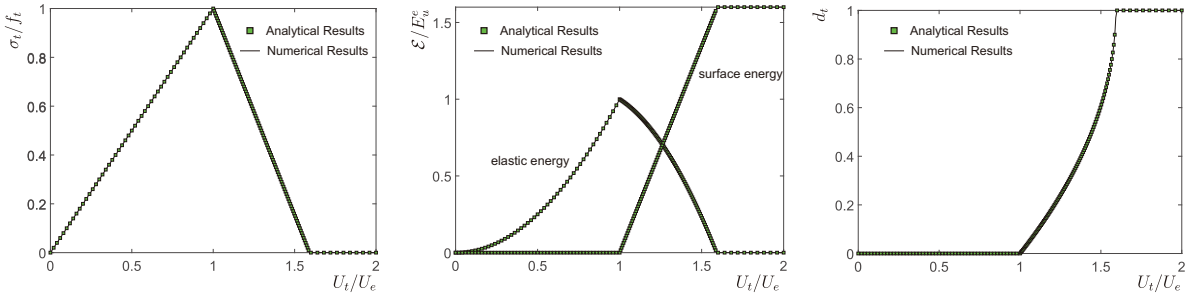

Figure 7: Load-displacement response (σ_t–U_t), evolution of the elastic and surface energies ($\mathcal{E}$-U_t) and phase field-displacement relation (d_t–U_t). f_t and U_e denote the elastic stress and the displacement limit in Equation (21), respectively.

Case 1: bar length $L = 5 < \min\left(L_b^1, L_b^2\right)$. The bar now deforms homogeneously. For the damage phase $t \geq t_e$, the homogeneous solution reads:

$$\frac{\sigma_t}{f_t} = \frac{2\,(U_t/U_e) - m}{2 - m} \quad d_t = 1 - \sqrt{\frac{2\,(U_t/U_e) - m}{2 - m}} \quad \frac{E_u^t}{E_u^e} = \frac{U_t}{U_e}\frac{2\,(U_t/U_e) - m}{2 - m} \quad \frac{E_s^t}{E_u^e} = \frac{m - mU_t/U_e}{2 - m} \tag{63}$$

with $E_u^e = E_0 U_e^2/2L$ being the elastic energy limit at t_e, $U_e = f_t L/E_0$ being the end displacement for the elastic limit, and m a coefficient, cf. Table 1.

Figure 7 shows a good agreement between the analytical and the numerical results. There exists an elastic phase when $U_t \leq U_e$. Then, there is no evolution of the phase field and of the surface energy, but only of the elastic energy. Right after $U_t = U_e$, the bar is in a stress-softening state. The stress and the surface energy have a linear relation with the displacement U_t, while the elastic energy shows a quadratic relation.

Case 2: bar length $\max\left(L_b^1, L_b^2\right) < L = 15 < L_u$. Under this condition, the bar will lose stability and will be damaged directly after $t = t_e$. In the damage phase $t \geq t_e$, the non-homogeneous solution reads:

$$\frac{\sigma_t}{f_t} = \frac{(U_t/U_e) - \zeta}{1 - \zeta} = 1 - \frac{\delta}{\delta_c} \quad d_{\mathrm{m}}^t = \frac{1 - (U_t/U_e)}{1 - \zeta} \quad \frac{E_u^t}{E_u^e} = \frac{U_t}{U_e}\frac{(U_t/U_e) - \zeta}{1 - \zeta} \quad \frac{E_s^t}{E_u^e} = \frac{f_t\delta}{2E_u^e} = \zeta\frac{1 - (U_t/U_e)}{1 - \zeta} \tag{64}$$

with $\zeta = 2\ell_{\mathrm{ch}}/L$, $U_e = f_t L/E_0$, $E_u^e = E_0 U_e^2/2L$ and $\delta_c = 2\mathcal{G}_c/f_t$. Obviously, the stress, the phase field and the surface energy increase linearly with U_t.

Figure 8 shows the results of numerical simulations and analytical formulations. A good agreement is obtained except for a small discrepancy due to ℓ and η being non-zero. The bar does not exhibit snapback behaviour in this case ($L < L_u = 2\ell_{\mathrm{ch}}$). Structural softening is observed, see Figure 8(a). The stress in the softening part is always $\sigma_t < f_t$. Crack nucleation will occur when $\sigma_t = 0$, see Figures 8(a)/(c). Apparently, the stress criterion in Equation (55b) does not apply. However, the energy criterion in Equation (55a) applies, see Figures 8(a)/(b). The elastic and surface energies evolve smoothly under a monotonically increasing load. This justifies the choice of $\max_{x\in(0,L]} d\,(x) = 1$ as the crack nucleation indicator rather than an energy jump, cf. Section 4.5. Figure 8(d) presents the stress-separation curve. Obviously, it mimics a linear cohesive zone law with a distinct surface energy $\mathcal{G} = E_s$, cf. Equations (48) and (49). The surface energy E_s increases linearly with δ, different from Equation (3). It takes the form of $\mathcal{G}\,(\delta)$ in the

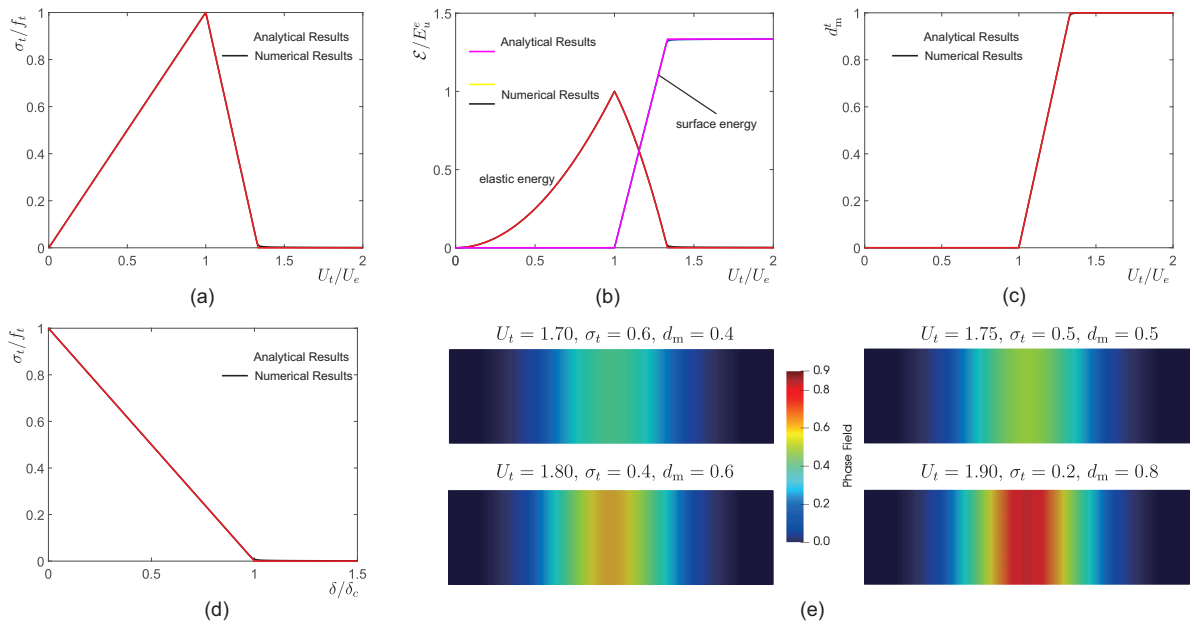

Figure 8: (a) Load-displacement response (σ_t–U_t), (b) Evolution of the elastic and surface energies ($\mathcal{E}$–U_t), (c) Phase field-displacement relation (d^t_{m}–U_t), (d) Stress-displacement jump relation, (e) Contour plot of the phase field d for different load steps. d^t_{m} is the maximum phase field along the plate at t, $U_e = f_t L/E_0$ is the limit of the 'elastic' displacement in Equation (21), $E^e_u = E_0 U_e^2/2L$ is the limit of the elastic energy at t_e, δ and $\delta_c = 2\mathcal{G}_c/f_t$ denote the displacement jump and the ultimate displacement jump in Equation (45), respectively.

Dugdale's cohesive relation (Equation (2)) with a reduced fracture strength $f_t/2$. Due to the softening, the phase field evolves with an increasing value of U_t, while the stress decreases, see Figures 8(c)/(e).

Case 3: bar length $L_u < L = 25$. The bar will now lose stability and exhibit a snapback right after $t = t_e$, see Figure 9. In the Figure, we compared analytical solutions, cf. Equation (64), with numerical simulations. Again, the slight difference at the tail in each figure is due ℓ and η being non-zero. Due to the snapback, the maximum elastic energy is bigger than the maximum surface energy, Figure 9(b). The necessary conditions for crack nucleation are complied with, see Equation (55). In the damage phase, the stress reduces with a decreasing value of U_t, while the phase field continues to evolve, see Figures 9(a), (c) and (e). As for model AT1, the stress-separation relation in Figure 9(d) is identical to that in Figure 8(d).

7. Concluding remarks

We have studied the construction of cohesive-zone models in a one-dimensional setting. With a proper choice of the degradation function and the homogeneous energy dissipation function, different cohesive-zone laws can be obtained. We have considered a 1D bar with stress softening. The bar will undergo homogeneous deformations at any given time if the bar length is less than a state dependent critical value. Otherwise, a non-homogeneous solution will be obtained due to loss of stability. Such an inhomogeneous solution leads to the response of cohesive-zone models. If we consider a sufficiently long bar, snapback behaviour will occur, which will lead to a sudden drop of surface energy. A phase-field method can partly reconstruct the cohesive-zone response, including the traction-separation law. This does not hold, however, for the dissipated energy. The derived model combines properties of the Barenblatt and the Dugdale versions of the cohesive-zone model. For a one-dimensional problem, crack nucleation is governed by a strength criterion and a toughness criterion, depending on the bar length. We compared the 1D analytical results with the numerical solutions in a 2D setting, yielding excellent agreement.

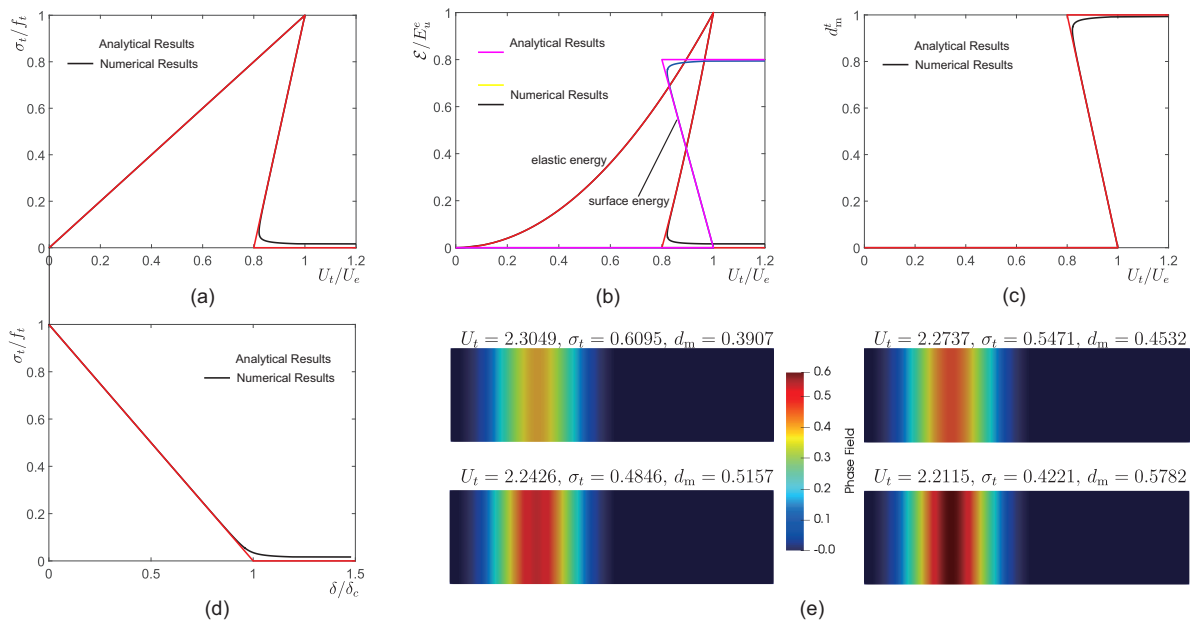

Figure 9: (a) Load-displacement response (σ_t-U_t), (b) Evolution of the elastic and surface energies ($\mathcal{E}$-U_t), (c) Phase field-displacement relation (d_m^t-U_t), (d) Stress-displacement jump (separation) relation, (e) Contour plot of the phase field d for different load steps. d_m^t is the maximum phase field along the plate at t, $U_e = f_t L/E_0$ is the limit of the 'elastic' displacement, cf. Equation (21), $E_u^e = E_0 U_e^2/2L$ is the limit of the elastic energy at t_e, δ and $\delta_c = 2\mathcal{G}_c/f_t$ denote the displacement jump and the ultimate displacement jump in Equation (45), respectively.

Acknowledgement

Financial support from the European Research Council (ERC Advanced Grant 664734 PoroFrac) is gratefully acknowledged.

References

[1] D. Ngo, A. C. Scordelis, Finite element analysis of reinforced concrete beams, Journal of the American Concrete Institute 64 (1967) 152–163.

[2] Y. R. Rashid, Analysis of reinforced concrete pressure vessels, Nuclear Engineering and Design 7 (1968) 334–344.

[3] R. de Borst, Some recent issues in computational failure mechanics, International Journal for Numerical Methods in Engineering 52 (2001) 63–95.

[4] R. de Borst, J. J. C. Remmers, A. Needleman, M. A. Abellan, Discrete vs smeared crack models for concrete fracture: bridging the gap, International Journal for Numerical and Analytical Methods in Geomechanics 28 (2004) 583–607.

[5] A. R. Ingraffea, V. Saouma, Numerical modelling of discrete crack propagation in reinforced and plain concrete, in: Fracture Mechanics of Concrete, Martinus Nijhoff Publishers, Dordrecht, 1985, pp. 171–225.

[6] T. Belytschko, T. Black, Elastic crack growth in finite elements with minimal remeshing, International Journal for Numerical Methods in Engineering 45 (1999) 601–620.

[7] N. Moës, J. Dolbow, T. Belytschko, A finite element method for crack growth without remeshing, International Journal for Numerical Methods in Engineering 46 (1999) 131–150.

[8] T. P. Fries, T. Belytschko, The extended/generalized finite element method: An overview of the method and its applications, International Journal for Numerical Methods in Engineering 84 (2010) 253–304.

[9] S. Secchi, L. Simoni, B. A. Schrefler, Mesh adaptation and transfer schemes for discrete fracture propagation in porous materials, International Journal for Numerical and Analytical Methods in Geomechanics 31 (2007) 331–345.

[10] L. Chen, C. V. Verhoosel, R. de Borst, Discrete fracture analysis using locally refined T-splines, International Journal for Numerical Methods in Engineering 116 (2018) 117–140.

[11] L. Chen, F. J. Lingen, R. de Borst, Adaptive hierarchical refinement of nurbs in cohesive fracture analysis, International Journal for Numerical Methods in Engineering 112 (2017) 2151–2173.

[12] J.-W. Chen, X.-P. Zhou, The enhanced extended finite element method for the propagation of complex branched cracks, Engineering Analysis with Boundary Elements 104 (2019) 46–62.

[13] R. de Borst, M. A. Gutiérrez, A unified framework for concrete damage and fracture models including size effects, International Journal of Fracture 95 (1999) 261–277.

[14] G. A. Francfort, J. J. Marigo, Revisiting brittle fracture as an energy minimization problem, Journal of the Mechanics and Physics of Solids 46 (1998) 1319–1342.

[15] B. Bourdin, G. A. Francfort, J. J. Marigo, The variational approach to fracture, Journal of Elasticity 91 (2008) 5–148.
[16] C. Miehe, M. Hofacker, F. Welschinger, A phase field model for rate-independent crack propagation: Robust algorithmic implementation based on operator splits, Computer Methods in Applied Mechanics and Engineering 199 (2010) 2765–2778.
[17] C. Miehe, F. Welschinger, M. Hofacker, Thermodynamically consistent phase-field models of fracture: Variational principles and multi-field FE implementations, International Journal for Numerical Methods in Engineering 83 (2010) 1273–1311.
[18] R. de Borst, C. V. Verhoosel, Gradient damage *vs* phase-field approaches for fracture: Similarities and differences, Computer Methods in Applied Mechanics and Engineering 312 (2016) 78–94.
[19] B. Bourdin, G. A. Francfort, J. J. Marigo, Numerical experiments in revisited brittle fracture, Journal of the Mechanics and Physics of Solids 48 (2000) 797–826.
[20] C. Hesch, S. Schuß, M. Dittmann, M. Franke, K. Weinberg, Isogeometric analysis and hierarchical refinement for higher-order phase-field models, Computer Methods in Applied Mechanics and Engineering 303 (2016) 185–207.
[21] J. Y. Wu, A unified phase-field theory for the mechanics of damage and quasi-brittle failure, Journal of the Mechanics and Physics of Solids 103 (2017) 72–99.
[22] L. Wang, X. Zhou, Phase field model for simulating the fracture behaviors of some disc-type specimens, Engineering Fracture Mechanics 226 (2020) 106870.
[23] B. Li, C. Peco, D. Millán, I. Arias, M. Arroyo, Phase-field modeling and simulation of fracture in brittle materials with strongly anisotropic surface energy, International Journal for Numerical Methods in Engineering 102 (2015) 711–727.
[24] L. Chen, B. Li, R. de Borst, Adaptive isogeometric analysis for phase-field modeling of anisotropic brittle fracture, International Journal for Numerical Methods in Engineering 121 (2020) 4630–4648.
[25] L. Chen, B. Li, R. de Borst, The use of Powell-Sabin B-Splines in a higher-order phase-field model for crack kinking, Computational Mechanicsdoi:10.1007/s00466-020-01923-0.
[26] C. V. Verhoosel, R. de Borst, A phase-field model for cohesive fracture, International Journal for Numerical Methods in Engineering 96 (2013) 43–62.
[27] J. Vignollet, S. May, R. de Borst, C. V. Verhoosel, Phase-field models for brittle and cohesive fracture, Meccanica 49 (2014) 2587–2601.
[28] S. May, J. Vignollet, R. de Borst, A numerical assessment of phase-field models for brittle and cohesive fracture: γ-convergence and stress oscillations, European Journal of Mechanics A/Solids 52 (2015) 72–84.
[29] Y. Ghaffari Motlagh, R. de Borst, Considerations on a phase-field model for adhesive fracture, International Journal for Numerical Methods in Engineering 121 (2020) 2946–2963.
[30] T. T. Nguyen, J. Yvonnet, Q.-Z. Zhu, M. Bornert, C. Chateau, A phase-field method for computational modeling of interfacial damage interacting with crack propagation in realistic microstructures obtained by microtomography, Computer Methods in Applied Mechanics and Engineering 312 (2016) 567–595.
[31] S. Conti, M. Focardi, F. Iurlano, Phase field approximation of cohesive fracture models, Annales de l'Institut Henri Poincaré C, Analyse Non Linéaire 33 (2016) 1033–1067.
[32] F. Freddi, G. Royer-Carfagni, Regularized variational theories of fracture: a unified approach, Journal of the Mechanics and Physics of Solids 58 (2010) 1154–1174.
[33] C. Chukwudozie, B. Bourdin, K. Yoshioka, A variational phase-field model for hydraulic fracturing in porous media, Computer Methods in Applied Mechanics and Engineering 347 (2019) 957–982.
[34] K. Yoshioka, D. Naumov, O. Kolditz, On crack opening computation in variational phase-field models for fracture, Computer Methods in Applied Mechanics and Engineering 369 (2020) 113210.
[35] D. S. Dugdale, Yielding of steel sheets containing slits, Journal of the Mechanics and Physics of Solids 8 (1960) 100–104.
[36] G. I. Barenblatt, The mathematical theory of equilibrium cracks in brittle fracture, Advances in Applied Mechanics 7 (1962) 55–129.
[37] X. P. Xu, A. Needleman, Void nucleation by inclusion debonding in a crystal matrix, Modelling and Simulation in Materials Science and Engineering 1 (1993) 111–132.
[38] F. Fathi, L. Chen, R. de Borst, Extended isogeometric analysis for cohesive fracture, International Journal for Numerical Methods in Engineering 121 (2020) 4584–4613.
[39] K. Pham, H. Amor, J.-J. Marigo, C. Maurini, Gradient damage models and their use to approximate brittle fracture, International Journal of Damage Mechanics 20 (2011) 618–652.
[40] E. Lorentz, S. Cuvilliez, K. Kazymyrenko, Convergence of a gradient damage model toward a cohesive zone model, Comptes Rendus Mécanique 339 (2011) 20–26.
[41] K. Pham, J.-J. Marigo, C. Maurini, The issues of the uniqueness and the stability of the homogeneous response in uniaxial tests with gradient damage models, Journal of the Mechanics and Physics of Solids 59 (2011) 1163–1190.
[42] J.-Y. Wu, J.-F. Qiu, V. P. Nguyen, T. K. Mandal, L.-J. Zhuang, Computational modeling of localized failure in solids: XFEM vs PF-CZM, Computer Methods in Applied Mechanics and Engineering 345 (2019) 618–643.
[43] L. Ambrosio, V. M. Tortorelli, Approximation of functionals depending on jumps by elliptic functionals via Γ-convergence, Communications on Pure and Applied Mathematics 43 (1991) 999–1036.
[44] J.-J. Marigo, C. Maurini, K. Pham, An overview of the modelling of fracture by gradient damage models, Meccanica 51 (2016) 3107–3128.
[45] K. Pham, J.-J. Marigo, From the onset of damage to rupture: construction of responses with damage localization for a general class of gradient damage models, Continuum Mechanics and Thermodynamics 25 (2013) 147–171.
[46] E. Tanné, T. Li, B. Bourdin, J.-J. Marigo, C. Maurini, Crack nucleation in variational phase-field models of brittle fracture, Journal of the Mechanics and Physics of Solids 110 (2018) 80–99.
[47] D. Leguillon, Strength or toughness? a criterion for crack onset at a notch, European Journal of Mechanics-A/Solids 21 (2002) 61–72.
[48] S. May, J. Vignollet, R. de Borst, A new arc-length control method based on the rates of the internal and the dissipated energy, Engineering Computations 33 (2016) 100–115.
[49] T. Gerasimov, L. De Lorenzis, On penalization in variational phase-field models of brittle fracture, Computer Methods in Applied Mechanics and Engineering 354 (2019) 990–1026.

[50] S. May, J. Vignollet, R. de Borst, Powell-Sabin B-splines and unstructured standard T-splines for the solution of Kichhoff-Love plate theory using Bézier extraction, International Journal for Numerical Methods in Engineering 107 (2016) 205–233.
[51] S. May, R. de Borst, J. Vignollet, Powell-Sabin B-splines for smeared and discrete approaches to fracture in quasi-brittle materials, Computer Methods in Applied Mechanics and Engineering 307 (2016) 193–214.
[52] L. Chen, R. de Borst, Cohesive fracture analysis using powell-sabin b-splines, International Journal for Numerical and Analytical methods in Geomechanics 43 (2019) 625–640.
[53] C. Geuzaine, J.-F. Remacle, Gmsh: A 3-D finite element mesh generator with built-in pre-and post-processing facilities, International Journal for Numerical Methods in Engineering 79 (2009) 1309–1331.
[54] A. Mesgarnejad, B. Bourdin, M. M. Khonsari, Validation simulations for the variational approach to fracture, Computer Methods in Applied Mechanics and Engineering 290 (2015) 420–437.